Enhanced Isochoric Heating from Fast Electrons Produced by High-Contrast, Relativistic-Intensity Laser Pulses

F. Perez,[1,*] L. Gremillet,[2] M. Koenig,[1] S. D. Baton,[1] P. Audebert,[1] M. Chahid,[1] C. Rousseaux,[2] M. Drouin,[2] E. Lefebvre,[2] T. Vinci,[2] J. Rassuchine,[3] T. Cowan,[3] S. A. Gaillard,[3,4,5] K. A. Flippo,[4] and R. Shepherd[6]

[1]*Laboratoire pour l'Utilisation des Lasers Intenses, UMR 7605 CNRS-CEA-X-Paris VI, Ecole Polytechnique, Palaiseau, France*
[2]*CEA, DAM, DIF, F-91297 Arpajon Cedex, France*
[3]*Forschungszentrum Dresden-Rossendorf, POB 510119, 01314 Dresden, Germany*
[4]*Los Alamos National Laboratory, Los Alamos, New Mexico 87545, USA*
[5]*Department of Physics, University of Nevada, Reno, Nevada 89557, USA*
[6]*Lawrence Livermore National Laboratory, Livermore, California 94550, USA*

(Received 19 May 2009; published 25 February 2010)

Thin, mass-limited targets composed of V/Cu/Al layers with diameters ranging from 50 to 300 μm have been isochorically heated by a 300 fs laser pulse delivering up to 10 J at 2×10^{19} W/cm^2 irradiance. Detailed spectral analysis of the Cu x-ray emission indicates that the highest temperatures, of the order of 100 eV, have been reached when irradiating the smallest targets with a high-contrast, frequency-doubled pulse despite a reduced laser energy. Collisional particle-in-cell simulations confirm the detrimental influence of the preformed plasma on the bulk target heating.

DOI: 10.1103/PhysRevLett.104.085001 PACS numbers: 52.50.Jm, 52.38.Kd, 52.70.La

High-energy density physics (HEDP) in the laboratory is an emerging field enabled by the development of pulsed power facilities over the past two decades [1]. A central topic of this field is the study of warm dense matter (WDM), i.e., the long poorly understood region of the material phase diagram located between condensed matter and plasma states. Since the validity of even state-of-the-art atomic physics models and simulation tools is not ensured in this frontier domain, there is a critical need for experimental data. In this respect, high power lasers are particularly attractive because of their ability to generate WDM states and diagnose their properties with unrivalled time and space resolutions.

A major challenge for the understanding of WDM lies in uniformly heating solid-density matter up to 10–100 eV, which may then serve as a valuable test bed for atomic physics models. This so-called isochoric heating is now within the reach of a new class of ultra-high-intensity, high-energy lasers, as recently demonstrated via either direct laser-solid interaction [2,3] or using laser-generated high-energy protons [4]. Indeed, provided these laser pulses are short enough and highly contrasted, they interact with the dense target before any significant hydrodynamical expansion arises. Through their subsequent conversion into penetrating energetic particles or radiation, short laser pulses may therefore constitute efficient tools for fast (i.e., ps-time scale) in-depth heating of solid-density matter.

A well-known feature of laser-solid interaction at ultra-high intensities is that most of the laser-accelerated electrons remain trapped inside the electrostatic potential well of the slowly expanding target [5–7]. Owing to this efficient confinement, reduced-mass targets (i.e., significantly smaller than the fast electrons range) are expected to reach higher temperatures than infinite targets for a fixed input energy [8].

In this Letter, we demonstrate the benefit of using a frequency-doubled, ultra-high-intensity laser pulse for the isochoric heating of reduced-mass targets. The LULI 100 TW laser system was focused with a $f/3$ off-axis parabola onto disc-shaped solid targets. The normally incident pulse was approximately 300 fs long and delivered an energy of $\sim$10 J within a $\sim$12 μm FWHM spot, yielding an intensity of $\sim 2 \times 10^{19}$ W/cm^2. For a wavelength of 1.057 μm ($1\omega_0$), the amplified stimulated emission (ASE) pedestal was characterized by a contrast ratio ranging from 10^6 to 10^7 and a typical duration of 500 ps. Frequency doubling to 0.528 μm ($2\omega_0$) was achieved using a KDP crystal with $\sim$50% conversion efficiency, giving an energy $\sim$5 J. The focal spot was then measured to be $\sim$8 μm. The multilayer targets were composed of 5 μm Cu and 5 μm Al with diameters varying from 50 to 300 μm. The front (Cu) layer was coated with a thin (200 nm) V layer in order to prevent direct heating from the laser.

Several x-ray diagnostics were implemented in order to infer the electron transport in the target and its heating. Two spherically bent quartz crystals with 1.541 Å interatomic distance and 380 mm radii of curvature produced rear-view and side-view monochromatic images [9] of the target around the CuK_α lines (8.05 keV) with a spectral acceptance of $\sim$10 eV and a spatial resolution of $\sim$20 μm. In addition, a cylindrically bent quartz crystal in a von Hamos configuration with a 1.012 Å interatomic distance produced space- and time-integrated spectra around the CuK_α line with a resolution $\Delta E < 5$ eV at first order of Bragg reflection. All x-ray diagnostics were

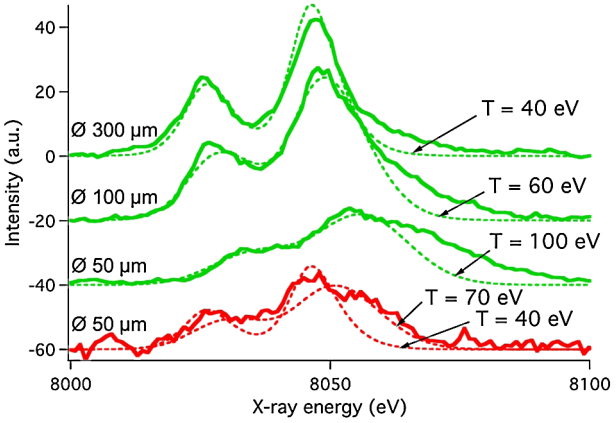

FIG. 1 (color online). CuK_α spectra for different target diameters irradiated at $2\omega_0$ (green, top-three curves) and $1\omega_0$ (red, bottom curve). The dashed lines correspond to the FLYCHK profiles for varying temperatures.

coupled with x-ray CCD cameras except for the von Hamos spectrometer, which used imaging plates instead.

Figure 1 displays typical spectra obtained for different target and laser parameters, in which the CuK_α doublet lines (centered at 8.048 and 8.028 keV at low temperatures) are clearly differentiated. The spectra suggest that a reduced target diameter leads to an increased thermal broadening of the CuK_α lines, which is indicative of higher temperatures in the Cu layer for smaller targets. This is shown in Fig. 1 in the case of $2\omega_0$ irradiation, but is also observed at $1\omega_0$. In order to quantify the target heating, we compared the measured profiles with those computed by the atomic code FLYCHK [10]. The CuK_α emission is modeled by adding a hot electron component to the thermal electron population. As suggested by the PIC simulations below, the hot electron fraction and temperature were varied from 0.1 to 1% and from 400 keV to 1.5 MeV, respectively, but the resulting spectral shape depends only very weakly on these parameters [11]. The input thermal electron temperature T is then adjusted in the code to best fit the experimental data, as shown in Fig. 1. Note that FLYCHK predicts that the line broadening becomes smaller than the spectrometer resolution for temperatures below 30 eV, which sets a lower limit for our diagnostic. The peak temperatures, of the order of 100 eV, are reached for the smallest targets. Nevertheless, the simulated spectra miss a high x-ray energy shoulder often seen in the measurements, due to the blue shift of the CuK_α line arising at high temperatures. A better reproduction of the experimental data would therefore require accounting for several plasma components of varying temperatures. Since our measurements are space and time integrated, this discrepancy indicates a nonuniform (in space and/or time) target heating. This is supported by the rear-view x-ray images of the target at $1\omega_0$ [Fig. 2(a)] and, to an even greater extent, at $2\omega_0$ [Fig. 2(b)]. The measured x-ray signal at $2\omega_0$ is twice brighter in the central spot and twice

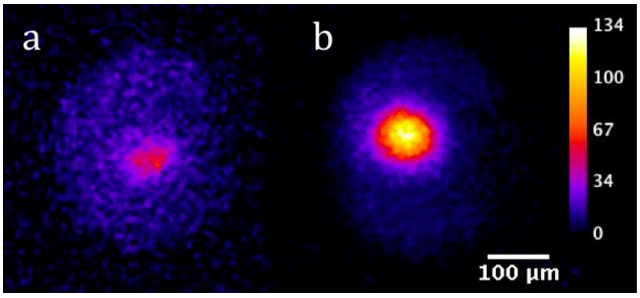

FIG. 2 (color online). Rear-view images at 8 keV of 300 μm diameter targets irradiated at $1\omega_0$ (a) and $2\omega_0$ (b).

weaker in the outer region than at $1\omega_0$, resulting in an overall equal integrated signal. This difference will be qualitatively explained further below.

The dependence of the mean target temperature upon the target size is roughly estimated as follows. Previous measurements [12] based on K-shell emission intensity and Monte Carlo modelling estimated 15 to 25% laser-to-hot-electron conversion efficiency, thus leading to a predicted total electron kinetic energy of the order of 1.5–2.5 J when operating at $1\omega_0$, and about half this value at $2\omega_0$. Note that accounting for ion expansion and resistive effects could lead to significantly increased conversion efficiencies [13]. Assuming perfect electron confinement and uniform heating, an average target temperature can then be directly deduced from the materials equation of state (EOS) using the SESAME tables [14].

The overall results are plotted in Fig. 3 for various target sizes and laser wavelengths. As expected, the target temperature rises for decreasing target sizes. The experimental values appear to be always below the predicted ones for small targets. This trend reverses for the largest targets, but the aforementioned nonuniformities, contrary to our assumption, may then be particularly pronounced. Moreover, except for the 300 μm targets, the measurements at $2\omega_0$ fall closer to the predictions than at $1\omega_0$, which provides evidence of a better coupling efficiency using frequency-

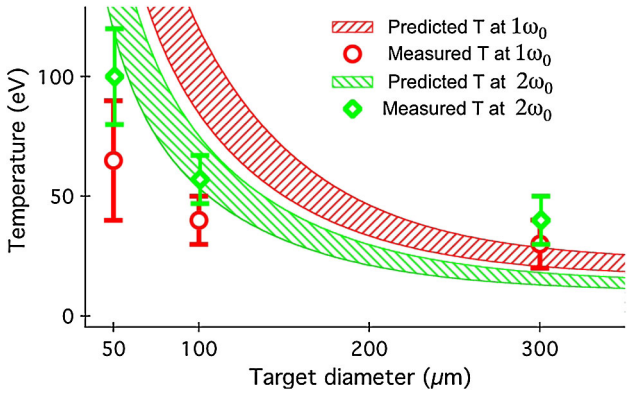

FIG. 3 (color online). Temperature measurements for varying target sizes at $1\omega_0$ and $2\omega_0$. EOS-predicted simple estimates are shown as hatched areas for a 15%-25% laser-to-hot-electron conversion efficiency.

doubling. In other words, energy losses are more important at $1\omega_0$. More surprisingly, the highest temperatures are obtained at $2\omega_0$ for the full range of target sizes investigated, despite an approximately halved laser energy compared to the $1\omega_0$ shots. This intriguing finding is illustrated in Fig. 1 in the case of a 50 μm diameter target, which is heated up to ~100 eV at $2\omega_0$ and only about half this value at $1\omega_0$. These observations point to the detrimental role of the ASE-generated preplasma at $1\omega_0$ in the coupling of the incident laser energy with the solid-density part of the target, as recently demonstrated with cone-guided targets [15–17]. The side-view x-ray images of Fig. 4 support the formation of a large-scale preplasma at $1\omega_0$, as they exhibit, in this case only, a strong emission extending tens of microns away from the solid-density region.

To investigate the influence of both the preplasma size and the laser wavelength on the fast electron-induced target heating, we have carried out two-dimensional (2D) collisional particle-in-cell (PIC) simulations with the 2D3V code CALDER [18]. We have considered a 50 μm-wide target made of preionized Cu^{15+} ion-electron plasma with initial temperature and maximum electron density equal to 10 eV and 400 n_c, respectively (n_c denotes the critical density at $\lambda_0 = 1.057$ μm). The target density is taken to be about one third of the solid density in order to ensure satisfactory energy conservation. The chosen (fixed) ionization degree permits to approximately reproduce the theoretical electrical resistivity of a solid-density Cu plasma in the temperature range $10\ \text{eV} < T < 1\ \text{keV}$ [19]. In the $1\omega_0$ case, the electron density profile along the laser direction (x axis) is taken from a DUED [20] hydrodynamical simulation of the preplasma generation by a 500 ps, 10^{13} W/cm^2 pedestal. The high-intensity pulse is injected from the left boundary with a 350 fs FWHM Gaussian temporal profile and a 12 μm FWHM Gaussian transverse profile, yielding a vacuum peak intensity times wavelength squared $I\lambda^2 = 1.8 \times 10^{19}$ W μm^2/cm^2. At $2\omega_0$, given the absence of data concerning the residual ASE, we have considered an exponential preplasma profile with a 0.1 μm scale-length. In addition to a 50% drop in laser energy, we have assumed a 250 fs duration and a 8 μm focal spot so as to account approximately for the expected spatial and temporal narrowing due to frequency doubling, thus leading to a reduced peak value $I\lambda^2 = 6.4 \times 10^{18}$ W μm^2/cm^2. In both the $1\omega_0$ and $2\omega_0$ cases, the total target mass is that of a uniform 10×50 μm^2, 400 n_c target. Relativistic binary collisions (both electron-ion and electron-electron) are modeled using the Monte Carlo method of Nanbu [21,22] and the cross sections calculated in Ref. [23].

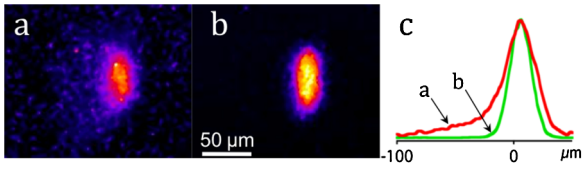

FIG. 4 (color online). Side-view images at 8 keV of 50 μm diameter targets irradiated at $1\omega_0$ (a) and $2\omega_0$ (b) and corresponding horizontal profiles (c). The laser comes from the left-hand side.

The mean energy of the cold part (<10 keV) of the electron distribution is displayed in Fig. 5 for both irradiation cases at $t = 400$ fs after the on-target pulse maximum. We verified the thermal character of this population by checking that its drift kinetic energy is but a small fraction of its total energy. The heating of the dense region is about twice higher at $2\omega_0$ [Fig. 5(a)] than at $1\omega_0$ [Fig. 5(b)]. Interestingly, Fig. 5 shows that the heating is more peaked in the central region at $2\omega_0$, which is consistent with the CuK_α images of Fig. 2. Yet this does not affect the isochoric character of the heating at $2\omega_0$ as the target profile remains essentially unperturbed. In contrast, at $1\omega_0$, the temperature profile proves strongly inhomogeneous in the longitudinal direction due to the varying target density. One should note that, owing to their simplified 2D slab geometry, which minimizes the effects of electron dilution, and to the neglected collisional ionization and underestimated initial target density, our simulations overestimate the target heating by more than an order of magnitude compared to the experimental measurements. The collisional simulations of Ref. [24] lead to a similar overestimate.

The differences in the bulk target heating for the two cases under consideration mostly stem from distinct fast electron sources as shown in Fig. 6, which plots the kinetic energy density of the hot (>10 keV) part of the electron distribution at the on-target laser peak. At $1\omega_0$, the hot electrons, created away from the target bulk [15], fill the subcritical plasma volume irradiated by the laser pulse and are injected as diverging filaments into the target bulk [Fig. 6(a)]. All their kinetic energy is transported by particles above 100 keV, with mean energy ~1.5 MeV. In contrast, at $2\omega_0$, a fairly collimated electron beam is accelerated from the localized absorption region [Fig. 6(b)]. However, the cold and hot electron populations are not clearly separated in this case, so that only 70% of its energy is carried by electrons above 100 keV with mean energy of ~370 keV. Although the steep density gradient yields a twofold decrease in the laser-to-hot electron conversion efficiency (~30% vs ~60%, as measured after the laser extinction), the reduced fast electron divergence and target

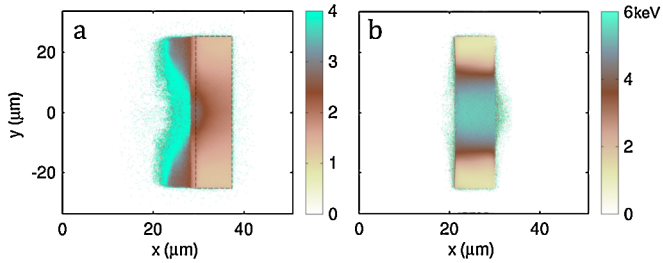

FIG. 5 (color online). Mean energy of bulk (<10 keV) electrons at $t = 400$ fs at $1\omega_0$ (a) and $2\omega_0$ (b). The dashed contour at $1\omega_0$ delimits the maximum density region.

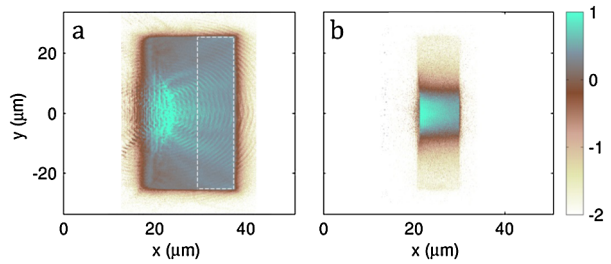

FIG. 6 (color online). Kinetic energy density (in $\log_{10}$ scale and normalized to $m_e c^2 n_c$) of the fast (>10 keV) electrons at $1\omega_0$ (a) and $2\omega_0$ (b). The dashed contour at $1\omega_0$ delimits the maximum density region.

volume enhance the energy density within the dense region by a factor ~1.5–2. The reduced collisional stopping range of the significant number of particles below 100 keV further contributes to the efficient target heating observed at $2\omega_0$. According to Ref. [25], the effective range in a 400 n_c, Cu^{15+} plasma is approximately 50 and 2700 μm for electron energies of 100 keV and 1.5 MeV, respectively.

Two further mitigating effects at $1\omega_0$ are worth mentioning. The first one is the increased ion acceleration occurring at $1\omega_0$, which amounts to ~16% of the laser absorption at $t = 400$ fs. This value exceeds the then reached laser-to-thermal-electron conversion efficiency (~ 5%), and is about twice higher than the value predicted at $2\omega_0$. It is almost equally split into forward- and backward-accelerated ions from the rear target surface and the preplasma, respectively. The second one is caused by the large, strongly magnetized plasma generated through the $\nabla T_e \times \nabla n_e$ effect [26] [Fig. 7(a)]. The quasistatic magnetic field reaches values greater than 10^4 T in the preformed plasma over distances larger than the corresponding gyroradius of ~ MeV electrons. As a result, we find that at the end of the interaction, about 25% of the total fast electron energy remains confined inside the magnetized region, whose mean energy is in the MeV range. At $2\omega_0$, a much thinner magnetized sheath forms [Fig. 7(b)], hence leading to a reduced magnetic retention effect [27]. Overall, the total energy transferred to the electrons within the nonmagnetized overcritical region amounts to about 40% and 25% of the laser energy at $1\omega_0$ and $2\omega_0$, respectively, at the end of the interaction.

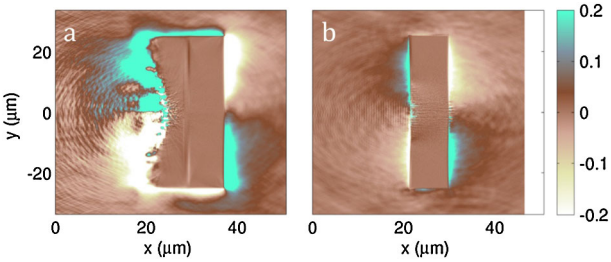

FIG. 7 (color online). Quasistatic magnetic field B_Z (normalized to $m_e\omega_0/e \sim 10^4$ T) at $t = 100$ fs after the pulse maximum at $1\omega_0$ (a) and $2\omega_0$ (b).

In conclusion, we have experimentally demonstrated the highly improved effectiveness of frequency-doubled laser pulses for the fast heating of mass-limited targets. Spectral analysis of the CuK_α emission indicates that 50 – μm-diameter targets can be heated above 100 eV with rather modest (~5 J) input laser energies at $2\omega_0$. In qualitative agreement with the experimental data, collisional PIC simulations reveal that the reduced beam divergence, mean energy, and magnetic field inhibition occurring at $2\omega_0$ contribute to increasing the hot electron energy density and the target heating.

The authors acknowledge D. Salzmann for his interest in this work and fruitful discussions. PIC simulations were performed using the computing facilities of CEA/CCRT. S. A. G. was supported by DOE grant DE-FC52-01NV14050 and travel supported by FZD. K. A. F. was supported by DOE contract # DE-AC52-06NA25396.

*frederic.perez@polytechnique.edu

[1] B. A. Remington, R. P. Drake, and D. D. Ryutov, Rev. Mod. Phys. **78**, 755 (2006).
[2] T. Ao *et al.*, Phys. Rev. Lett. **96**, 055001 (2006).
[3] A. Saemann *et al.*, Phys. Rev. Lett. **82**, 4843 (1999).
[4] P. K. Patel *et al.*, Phys. Rev. Lett. **91**, 125004 (2003).
[5] T. Nakamura and S. Kawata, Phys. Rev. E **67**, 026403 (2003).
[6] J. Myatt *et al.*, Phys. Plasmas **14**, 056301 (2007).
[7] S. D. Baton *et al.*, High Energy Density Phys. **3**, 358 (2007).
[8] P. M. Nilson *et al.*, Phys. Rev. E **79**, 016406 (2009).
[9] J. A. Koch *et al.*, Rev. Sci. Instrum. **74**, 2130 (2003).
[10] H. Chung *et al.*, High Energy Density Phys. **1**, 3 (2005).
[11] K. U. Akli *et al.*, Phys. Plasmas **14**, 023102 (2007).
[12] K. Yasuike *et al.*, Rev. Sci. Instrum. **72**, 1236 (2001).
[13] J. R. Davies, Phys. Rev. E **65**, 026407 (2002).
[14] See National Technical Information Service Document No. DE94011699 ("SESAME database" by J. D. Johnson, Los Alamos National Laboratory Report No. LA-UR-94-1451, 1994). Copies may be ordered from the National Technical Information Service, Springfield, VA 22161.
[15] S. D. Baton *et al.*, Phys. Plasmas **15**, 042706 (2008).
[16] L. V. Woerkom *et al.*, Phys. Plasmas **15**, 056304 (2008).
[17] J. Rassuchine *et al.*, Phys. Rev. E **79**, 036408 (2009).
[18] E. Lefebvre *et al.*, Nucl. Fusion **43**, 629 (2003).
[19] Y. T. Lee and R. M. More, Phys. Fluids **27**, 1273 (1984).
[20] S. Atzeni *et al.*, Comput. Phys. Commun. **169**, 153 (2005).
[21] K. Nanbu, Phys. Rev. E **55**, 4642 (1997).
[22] K. Nanbu and S. Yonemura, J. Comput. Phys. **145**, 639 (1998).
[23] N. E. Frankel, K. C. Hines, and R. L. Dewar, Phys. Rev. A **20**, 2120 (1979).
[24] Y. Sentoku *et al.*, Phys. Plasmas **14**, 122701 (2007).
[25] C. Deutsch *et al.*, Phys. Rev. Lett. **77**, 2483 (1996).
[26] D. W. Forslund and J. U. Brackbill, Phys. Rev. Lett. **48**, 1614 (1982).
[27] M. S. Wei *et al.*, Phys. Plasmas **15**, 083101 (2008).